Journal of African Earth Sciences 58 (2010) 547–552

Contents lists available at ScienceDirect

Journal of African Earth Sciences

journal homepage: www.elsevier.com/locate/jafrearsci

Lithology classification from seismic tomography: Additional constraints from surface waves

Jacek Stankiewicz *, Klaus Bauer, Trond Ryberg

Deutsches GeoForschungsZentrum GFZ, Section 2.2, Telegrafenberg, 14473 Potsdam, Germany

ARTICLE INFO

Article history:
Received 9 February 2010
Received in revised form 12 May 2010
Accepted 18 May 2010
Available online 31 May 2010

Keywords:
Surface waves
Tomography
Classification

ABSTRACT

An efficient way of interpreting a seismic profile cross-section is a joint interpretation of velocity models of different types of seismic waves. This study performs tomographic inversion of surface wave travel times observed during the seismic profile carried out in Namibia in the framework of the SIMBA project. The thus obtained surface wave velocity model is used to complement the previously computed P- and S-wave models. Profile sections characterised by similar seismic velocities are identified as lithological classes and remapped in model space. Two methods are used to identify such classes: a manual identification of high probability zones in a probability density function, and an automatic neural network approach. The results of these two methods are consistent with each other. The availability of the surface wave velocity model as additional independent physical parameter increases the correlation between the remapped lithological classes and the geological map, leading to the conclusion that the identified classes correspond to real geological formations.

1. Introduction

The SIMBA (Seismic Investigations of the Messum and Brandberg Areas) experiment was carried out in the framework of a larger project aimed at understanding magmatic processes related to the break-up of Western Godwana (e.g., Trumbull et al., 2000; Bauer et al., 2000). The seismic profile started near Cape Cross, and extended north-east for 75 km (Fig. 1). A rolling spread of 180 receivers was used at a total of 728 receiver locations, while 125 explosions fired from 9 m boreholes were used as sources. More detailed information regarding the experiment is given by Bauer et al. (2003). The main target area of the profile was the Messum intrusive complex – one of several subvolcanic ring complexes in Namibia formed just prior to the onset of seafloor spreading (Ewart et al., 1998). Surrounding the complex are the metasediments and granites of the Pan-African Damara Belt, often covered by sandstone, mudstone, and basalt flows (Milner, 1997).

Bauer et al. (2003) identified first arrivals of refracted P- and S-waves, and performed tomographic inversion on the two independent sets of travel times. The fact that these models were calculated independently of each other makes it possible to analyse the spatial distribution of the velocities, as well as of the Poisson's ratio, σ. Such an analysis targets the mapping of different lithological classes beneath the profile. In this study we identify surface waves in the recorded data, and use tomographic inversion to compute surface wave velocity models. While an analysis of P-wave velocity and Poisson's ratio has been done previously (Bauer et al., 2003), the accuracy in identifying lithological classes, and matching them to real geological formations, is increased by adding surface wave velocity as an additional independent parameter.

2. Surface wave tomography

As well as direct P- and S-waves, surface wave arrivals can be seen on a number of recorded traces (Fig. 2). As these arrivals are most prominent on the vertical components of the recordings, we interpret them as Rayleigh waves. Attempts to correlate variations in surface wave velocity with real geographical and geological features have been carried out for nearly half a century (e.g., Sato and Santo, 1969; Kausel et al., 1974). The surface wave velocities depend on similar factors to those influencing the S-wave velocity (most importantly the density of the medium), and with certain assumptions the S-wave velocity can be derived from the surface waves (Aki and Richards, 1980). These assumptions include a layered structure, or constant Poisson's ratio. Under particularly strict assumptions a linear relationship between the two can be assumed, approximating the surface wave velocity as 92% of the S-wave value (Xia et al., 1999). However, deviations from such relationships frequently occur; for example, surface waves are very sensitive to the medium's rigidity (e.g., Doyle, 1995). Such variations are likely to correspond to real geological features, which can be identified by incorporating surface wave velocities in the classification scheme.

* Corresponding author. Tel.: +49 331 2881223; fax: +49 331 2881266.
E-mail address: jacek@gfz-potsdam.de (J. Stankiewicz).

1464-343X/$ - see front matter © 2010 Elsevier Ltd. All rights reserved.
doi:10.1016/j.jafrearsci.2010.05.012

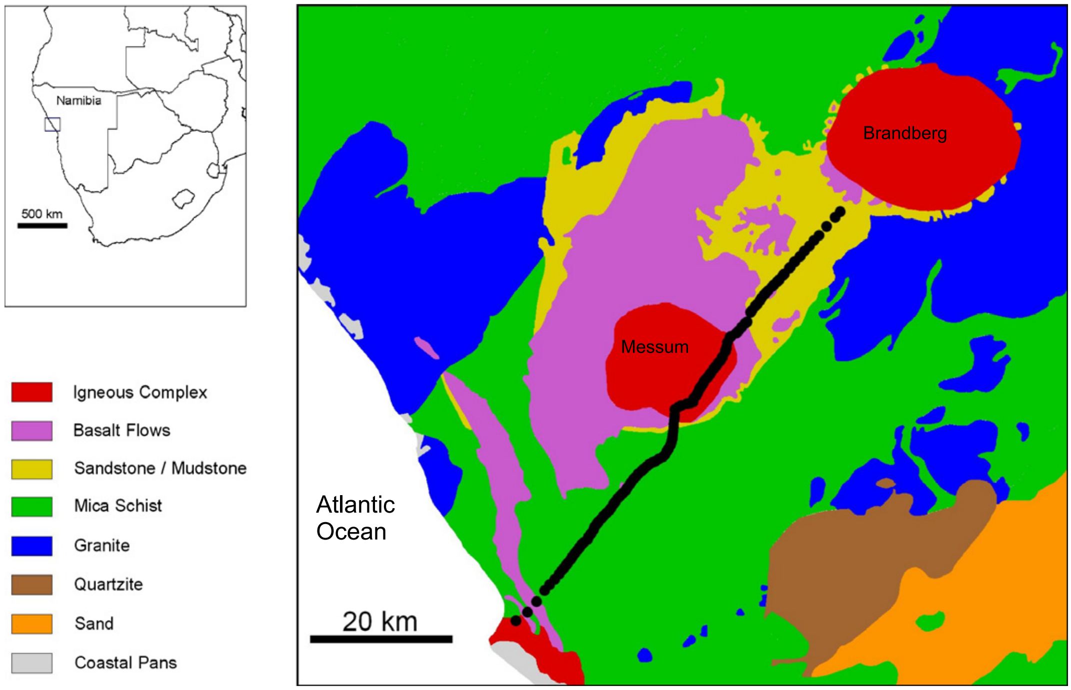

Fig. 1. Location of the SIMBA near-vertical seismic profile. The 125 shots are marked as black circles on the geological map of the region (simplified after Milner (1997)). The profile starts in the south-west near Cape Cross (km 0 in all further figures), crosses the Messum Igneous Complex, but for logistical reasons had to be stopped at km 73, just short of the bigger Brandberg Complex.

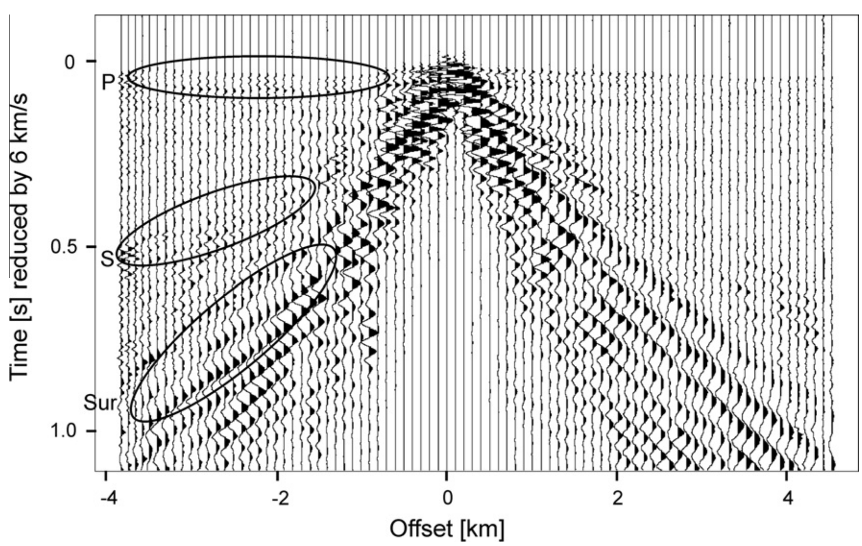

Fig. 2. Example of the raw signal recorded during a single shot. Traces were time-reduced by 6 km/s – thus the P-wave arrivals (marked with an ellipse) appear parallel to the x-axis. Slower arrivals of S-waves and surface waves (sur) also indicated with ellipses.

The velocity of surface waves is frequency dependent. Different frequencies f also sample different depths d (e.g., Ritzwoller and Levshin, 1998), with an approximate relationship being

$$d\ [\mathrm{m}] \approx \frac{1000\ \mathrm{m/s}}{f\ [\mathrm{Hz}]} \quad (1)$$

To explore this dependence of frequency, different sets of picks were made after the traces were subjected to different narrow band pass Ormsby filters. Six centre frequencies were used: 15 Hz, 10 Hz, 7 Hz, 5 Hz, 3.33 Hz and 2.5 Hz. Both higher and lower frequencies than ones listed here were also examined, but no significant surface wave arrivals could be detected. Using Eq. (1) above we can estimate that while the 15 Hz waves penetrate only the uppermost ~60–70 m, the 2.5 Hz signal samples up to a depth of ~400 m.

For each centre frequency arrival times of the surface wave were automatically picked. This was done by calculating the envelope of each filtered trace, and finding the location of its maximum along the segment corresponding to an arrival with a velocity between 1 and 3 km/s. Having obtained the arrival times, travel time tomography was used to calculate the group velocity of the particular frequency along the profile. For the tomographic inversion the Fast Marching Surface Tomography code (Rawlinson and Sambridge, 2005) was used. These inversions provided us with six

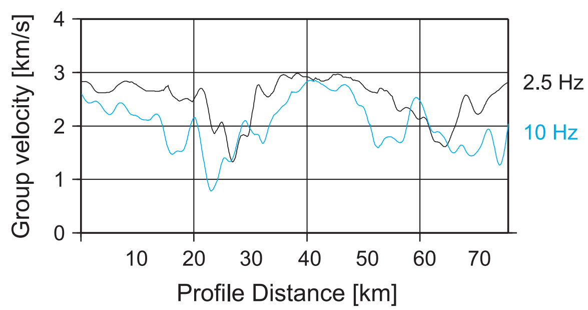

Fig. 3. Calculated group velocities of the 2.5 Hz (black) and 10 Hz (blue) surface waves along the profile, from south-west to north-east.

one-dimensional velocity models (one for each centre frequency). Group velocities of the 2.5 Hz and 10 Hz signals are illustrated in Fig. 3 as examples. Each of these models gives the distribution of average velocity down to a different depth. By successively stripping the shallow depth models (corresponding to higher frequencies), surface wave velocity distribution at depth as well as along profile can be estimated. For example, assume two one-dimensional velocity models v_1 and v_2 (both functions of distance along profile) exist for two centre frequencies $f_1 > f_2$. The model velocities give the average velocity between surface and the corresponding sampling depth, $d_1 < d_2$. The v_2 model is the weighed harmonic average of the velocity model v_1 and the velocity distribution between the depths d_1 and d_2, $v_{2'}$, which can be gives as

$$v_{2'} = \frac{d_2 - d_1}{\frac{d_2}{v_2} - \frac{d_1}{v_1}} \tag{2}$$

Performing this averaging scheme iteratively for lower centre frequency (greater sampling depth) one-dimensional velocity models, a two-dimensional model of surface wave velocity was computed. This is shown in Fig. 4.

3. Classification

Interpretation of seismic velocities in terms of lithology can be treated as a classification problem (e.g., Schalkoff, 1992). This approach involves categorising objects by assigning them to classes defined by limits of the measured physical parameters, in our case the various seismic velocities.

3.1. Manual classification using two parameters

When two independent parameters are available, classification can be performed manually. To achieve this, a probability density function (pdf) of the parameter distribution needs to be calculated using the values of the available parameters and their associated uncertainties. For example, to generate a pdf of P-wave and surface wave velocity distribution, a common grid needs to be constructed, with the values for v_p and v_{sur}, along with uncertainties δv_p and δv_{sur}, specified at each grid cell. For each model grid cell, i, assuming a normal error distribution, the pdf is given by:

$$pdf_i(v_p, v_{sur}) = \frac{1}{\sqrt{2\pi(\delta v_p)_i(\delta v_{sur})_i}} e^{-\frac{1}{2}\left[\frac{(v_p-(v_p)_i)^2}{\delta(v_p)_i^2} + \frac{(v_{sur}-(v_{sur})_i)^2}{\delta(v_{sur})_i^2}\right]} \tag{3}$$

And the complete pdf is given by the sum of individual functions generated from all available data pairs:

$$\mathrm{pdf}(v_p, v_{sur}) = \frac{1}{n}\sum_{i=1}^{n} pdf_i(v_p, v_{sur}) \tag{4}$$

A high value for this function indicates a high probability of a point in the model space having the corresponding values for P-wave and surface wave velocity.

Following the computation of the probability density function, a manual cluster analysis is performed to identify various classes. This involves identifying topologically continuous regions, or clusters, of high probability on the pdf. An important issue is the number of such clusters one attempts to identify. While it is important to identify all possible lithological classes, it is equally important to avoid attempts at interpretation of numerical artifacts. To identify the optimal number, we follow the technique of Bedrosian et al. (2007). In this method a function consisting of a sum of n Gaussian functions that best fit the computed pdf is calculated. The misfit between the original pdf and the Gaussian functions can then be calculated. With increasing n, the misfit will decrease, but above

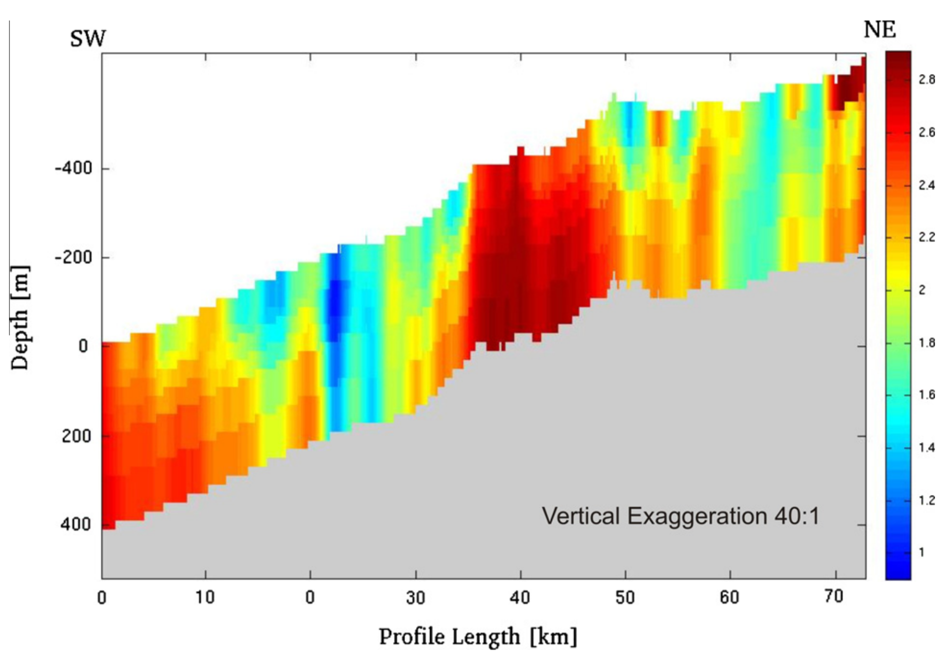

Fig. 4. The final surface wave velocity model along the profile.

a certain point this decrease will become very gradual. This point of the maximum curvature of the "*L*-curve" corresponds to the number of real classes that are likely to exist in the model.

The final step in the classification process is remapping the clusters into the original model space. This involves comparing the input parameter values (in our case P- and surface wave velocities) at each model grid cell to the parameter values defining the clusters, and assigning the grid cell to the cluster with matching, or closest, values. This provides the spatial distribution of clusters, which is essential for a lithologic interpretation.

3.2. Neural network approach for more than two parameters

The method discussed above does not use the information contained in the S-wave velocity model. However, incorporating a third parameter in the method discussed above would require the probability density function to be a function of three parameters, and clusters would need to be identified in three-dimensional space.

Instead, the neural network method is used. The technique used here was developed by Bauer et al. (2008), and only its overview will be presented here. The first phase of the analysis is the training. During this phase, a cell in parameter space (in our case, seismic velocity) is chosen at random, and a data vector is constructed using the values for each available parameter at the chosen cell. The dimension of this vector will correspond to the number of parameters available. When P-, S- and surface wave velocities are available, a three-dimensional vector will represent the velocities at the first iteration, $t = 1$:

$$\vec{x}(t) = [v_p(t), v_s(t), v_{sur}(t)]^T \tag{5}$$

This data vector is then used as input for a two-dimensional array of neurons. At the start of the training phase, each neuron i is associated with a three-dimensional model vector $\vec{m}_i(t)$ with randomly set values. The neuron b associated with a vector most similar to the input data vector is called the winning neuron, and is determined based on the condition:

$$\forall i, ||\vec{x}(t) - \vec{m}_b(t)|| \leqslant ||\vec{x}(t) - \vec{m}_i(t)|| \tag{6}$$

The model vectors associated with the neurons are then updated using the learning rule:

$$\vec{m}_i(t+1) = \vec{m}_i(t) + \lambda(t) * h_{b,i}(t) * (\vec{x}(t) - \vec{m}_i(t)) \tag{7}$$

where λ is the learning rate, chosen between 0 and 1 at the start and then logarithmically decreased at each successive iteration t, and h the Gaussian neighbourhood function centred at the winning neuron. The width of the Gaussian is also progressively decreased during the training. This way the array of neurons converges to what is known as the trained Kohonen layer (after Kohonen (1995)).

This layer can then be used to classify all data vectors. To visualise the variations of the model vectors, following the approach of Bauer et al. (2008) the total gradient of the Kohonen layer is calculated:

$$|\nabla\vec{m}_i| = \sqrt{\left(\frac{\delta\vec{m}_i}{\delta x}\right)^2 + \left(\frac{\delta\vec{m}_i}{\delta y}\right)^2} \tag{8}$$

where x and y represent the principal directions in the Kohonen layer. This gradient map will consist of regions with low gradient, corresponding to model vectors being similar to the neighbouring ones, separated by zones of high gradient, where significant changes between model vectors occur. This corresponds to clusters of similar model parameter values being separated by cluster borders. By treating the gradient map as a topographic image, the watershed segmentation algorithm (Vincent and Soille, 1991) can be used to identify the clusters (Bauer et al., 2008).

Following the definition of clusters, the winning neuron is determined for each vector. The cell from which the vector was computed is assigned to the cluster in which the winning neuron exists.

4. Results

4.1. Manual classification

The pdf correlating P-wave and surface wave velocity distribution is shown in Fig. 5. The P-wave velocities, as well as the corre-

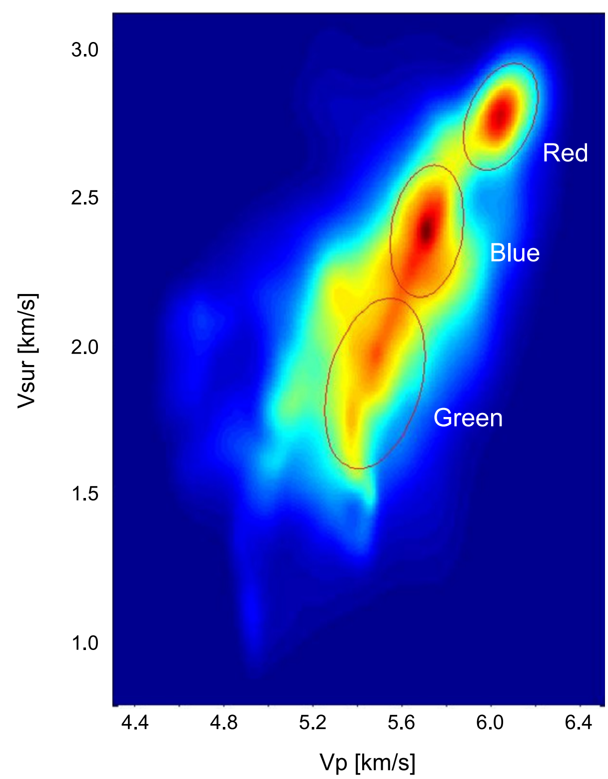

Fig. 5. Probability density function (pdf) correlating P-wave and surface wave velocities. Warm colours correspond to high probability of the corresponding pair of velocities existing in the models. The three most prominent clusters are marked with red ellipses. These are labeled with the colours corresponding to the remapping of clusters in Fig. 7.

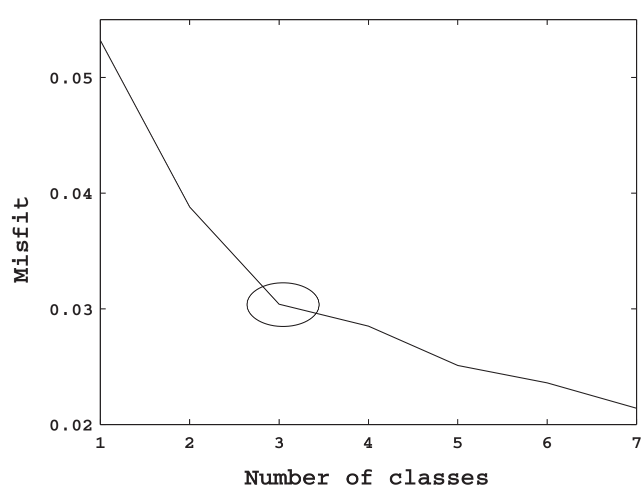

Fig. 6. The *L*-curve showing the misfit between the pdf in Fig. 5 and the best-fitting superposition of a number of Gaussian functions. Note the change in curvature around three Gaussian peaks.

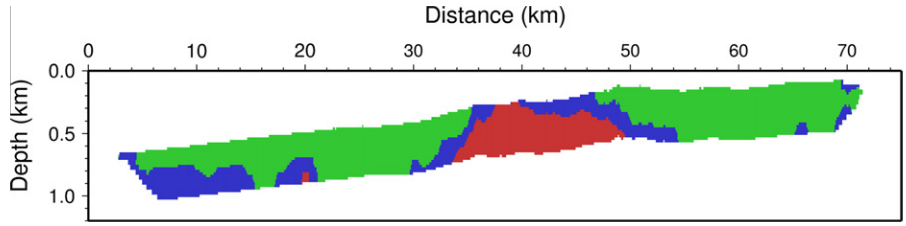

Fig. 7. Profile section showing the spatial distribution of the three clusters in Fig. 5. The red cluster corresponds to the Messum complex, the green to sandstones, mudstones and schists, and the blue to the underlying granites.

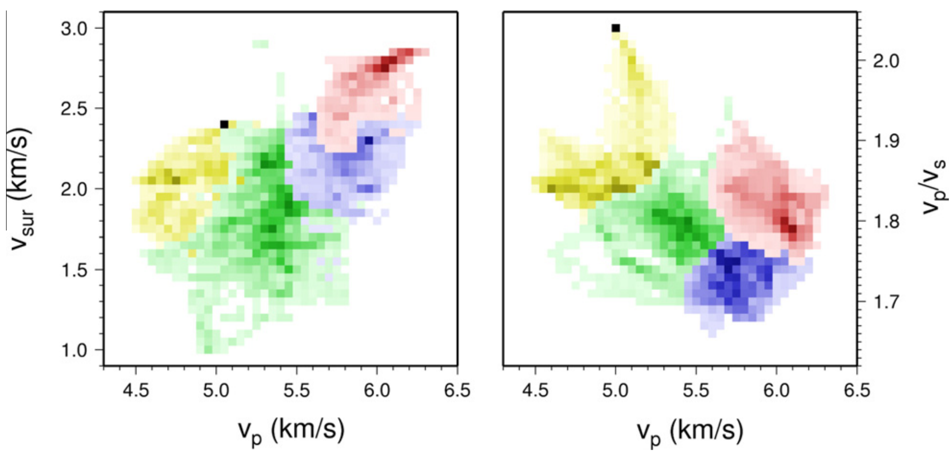

Fig. 8. Distribution of the four clusters in parameter space. For illustration purposes the three-dimensional clusters are projected into two-dimensional spaces: P-wave and surface wave (left); P-wave and ratio of P-wave/S-wave (right).

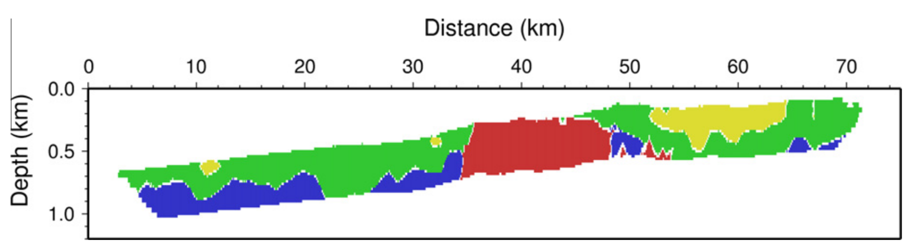

Fig. 9. Profile section showing the spatial distribution of the four clusters identified by the neural network algorithm. Distribution of the red (Messum) and blue (underlying granites) clusters is similar to Fig. 7, whereas the green cluster has been separated into yellow (sandstone and mudstone) and green (mica schists). Colours match the ones used to represent geological formations in Fig. 1.

sponding uncertainty, were computed by Bauer et al. (2003). The surface wave velocities were computed in this study using methods discussed earlier in this manuscript. As these methods allow only a qualitative analysis of the resolution, and the pdf calculation requires the uncertainty to be specified at each point, we have assumed the relative uncertainties to be twice as high as those in the P-wave model. Thus while acknowledging the surface wave model is not as well constrained as the P-wave model, we retain a realistic measure of uncertainty relative to the ray coverage and variations in signal quality. The *L*-curve analysis, showing how well the pdf can be fitted with an increasing number of clusters, is shown in Fig. 6. The change in curvature in the P-wave–surface wave misfit curve suggests three classes are present. This is consistent with a visual examination of the pdf, where three obvious clusters can be seen and manually picked (Fig. 5).

In order to interpret the classes, it is necessary to map them onto a 2-D depth section. Fig. 7 shows the section, with different colours being used to illustrate which of the three classes every point in model space fits into.[1]

4.2. Neural network approach

To incorporate the information contained in the S-wave model into our analysis, the multi-dimensional neural network approach was used. Four input parameters were used in the analysis: surface, P- and S-wave velocities, as well as the ratio between P- and S-wave velocities. The best results were obtained when the existence of four clusters was assumed – one more than for the two parameter analysis discussed earlier. This might have been expected, with the additional information coming from the S-wave

[1] For interpretation of colour in Figs. 1, 3–5 and 7–9, the reader is referred to the web version of this article.

model leading to a more detailed cluster identification. The distribution of the four clusters in parameter spaces is illustrated in Fig. 8, while their spatial distribution remapped onto the profile section is shown in Fig. 9.

5. Discussion and conclusions

The relocation of clusters onto the profile using the two different techniques (Figs. 7 and 9) is consistent. The one obvious difference is that what is illustrated as one cluster (in green in Fig. 7) has been subdivided into two (green and yellow in Fig. 9). This is the result of additional information provided by the S-wave velocities. The similarity between the figures does, however, confirm that when only two independent input parameters are available, manual cluster identification is a sufficiently reliable technique in our study area.

The most consistent feature on the remapped sections is the region mapped in red between profile km 35 and 50. This marks the location of the Messum intrusive complex (Fig. 1 – the colours on the geological map correspond to the clusters in Figs. 7 and 9), where high values are observed for all three types of seismic velocities (above 5.7–6.2 km/s for P-waves, 2.5–2.9 km/s for surface waves, 3.0–3.5 km/s for S-waves). These values are consistent with seismic velocities observed at similar intrusive complexes (e.g., Snyder et al., 2002).

The areas remapped in blue are likely to correspond to the Damara Belt granites. While the profile does not cross the surface exposure of these granites (Fig. 1), they are common in the study area, and are likely to underlie the geological formations that the profile does cross. This is consistent with Fig. 9, where the no regions remapped in blue exist on the surface. The blue regions at the surface in Fig. 7 all correspond to the Messum complex, and are clearly inconsistent with being remapped as Damara Belt rocks. As the two high-velocity clusters in Fig. 5 are very well defined, we believe this inconsistency is not a shortcoming of the manual cluster identification process, but a result of the lack of information regarding the S-wave velocity as an input parameter.

The cluster remapped in green in Fig. 7 can be divided into two distinct clusters when S-wave velocity information is available. Thus in Fig. 9 areas remapped in green, and in yellow, can be seen. These both have surface wave velocities below 2.4 km/s, as well as P-wave velocities under 5.6 km/s. However, a division can be made across around 1.80–1.85 for the ratio of P-wave to S-wave velocities, with regions exhibiting a higher ratio (lower S-wave velocity) corresponding to the yellow cluster, and the lower ratio (higher S-wave velocity) to the green. This correlates with the geological map, with the green cluster corresponding to the Mica Schist, and the yellow to the Sandstone and Mudstone formations. No cluster that would correlate to the basalt flows has been observed – these are likely to be too thin to have a resolvable signature in the velocity models.

In conclusion, we have reanalyzed the seismic data from the SIMBA experiment, and successfully identified surface wave arrivals. Using tomographic inversion of travel times of different group velocities, a surface wave velocity model was constructed for the uppermost 400 m. This model was combined with existing P- and S-wave velocity models. Our study showed that when two independent parameters (e.g., P-wave and surface wave velocities) are available, manual identification of clusters is a reliable tool for identifying lithological structures along the profile. When more than two parameters are available (e.g., additionally S-wave and/or Poisson's ratio), manual identification becomes much more difficult due to the visualisation problem of a function with more than two input parameters. For this reason an automatic neural network technique was used to identify clusters (corresponding to regions in the profile depth section) sharing specific parameters. These results do not contradict the manual process, but enhance it due to the fact more information is made available with the presence of additional input models.

Acknowledgments

The research presented here was funded by the Helmholtz-Russia Joint Research Groups (Project HRJRG-110). The SIMBA experiment was sponsored by the GeoForschungsZentrum Potsdam, using equipment from the Geophysical Instrument Pool Potsdam (GIPP).

The manuscript benefited from reviews by Ray Durrheim and George Smith.

References

Aki, K., Richards, P.G., 1980. Quantitative Seismology, Theory and Methods. W.H. Freeman, San Francisco.

Bauer, K., Neben, S., Schreckenberger, B., Emmermann, R., Hinz, K., Fechner, N., Gohl, K., Schulze, A., Trumbull, R.B., Weber, K., 2000. Deep structure of the Namibia continental margin as derived from integrated geophysical studies. Journal of Geophysical Research 105, 25829–25853.

Bauer, K., Schulze, A., Ryberg, T., Sobolev, S.V., Weber, M.H., 2003. Classification of lithology from seismic tomography: a case study from the Messum igneous complex, Namibia. Journal of Geophysical Research 108 (B3), 2152. doi:10.1029/2001JB001073.

Bauer, K., Pratt, R.G., Haberland, C., Weber, M., 2008. Neural network analysis of crosshole tomographic images: the seismic signature of gas hydrate bearing sediments in the Mackenzie Delta (NW Canada). Geophysical Research Letters 35, L19306. doi:10.1029/2008GL035263.

Bedrosian, P.A., Maercklin, N., Weckmann, U., Bartov, Y., Ryberg, T., Ritter, O., 2007. Lithology-derived structure classification from the joint interpretation of magnetotelluric and seismic models. Geophysical Journal International 170, 737–748.

Doyle, H., 1995. Seismology. John Wiley and Sons, Chichester, UK.

Ewart, A., Milner, S.C., Armstrong, R.A., Duncan, A.R., 1998. Etendeka volcanism of the Goboboseb mountains and Messum igneous complex, Namibia. Part I: geochemical evidence of Early Cretaceous Tristan plume melts and the role of crustal contamination in the Paraná–Etendeka CFB. Journal of Petrology 39, 191–225.

Kausel, E.G., Leeds, A.R., Knopoff, L., 1974. Variations of Rayleigh wave phase velocities across the Pacific Ocean. Science 186, 139–141.

Kohonen, T., 1995. Self-Organizing Maps. Springer, New York.

Milner, S.C., 1997. Geological map of Namibia, Omaruru, scale 1:250,000, sheet 2114. Ministry of Mines and Energy, Geological Survey of Namibia, Windhoek, Namibia.

Rawlinson, N., Sambridge, M., 2005. The fast marching method: an effective tool for tomographic imaging and tracking multiple phases in complex layered media. Exploration Geophysics 36, 341–350.

Ritzwoller, M.H., Levshin, A.L., 1998. Eurasian surface wave tomography: group velocities. Journal of Geophysical Research 103, 4839–4878.

Sato, Y., Santo, T., 1969. World-wide distribution of the group velocity of Rayleigh wave as determined by Dispersion Data. Bulletin of the Earthquake Research Institute 47, 31–41.

Schalkoff, R., 1992. Pattern Recognition: Statistical, Structural, and Neural Approaches. John Wiley and Sons, New York.

Snyder, D., Perron, G., Pflug, K., Stevens, K., 2002. New insights into the structure of the Sudbury Igneous Complex from downhole seismic studies. Canadian Journal of Earth Science 39, 943–951.

Trumbull, R.B., Emmermann, R., Buehn, B., Gerstenberger, H., Mingram, B., Schmitt, A., Volker, F., 2000. Insights on the genesis of the Cretaceous Damaraland igneous complexes in Namibia from Nd- and Sr-isotopic perspective. Communications of the Geological Survey of Namibia 12, 313–324.

Vincent, L., Soille, P., 1991. Watersheds in digital spaces: an efficient algorithm based on immersion simulation. IEEE Transactions on Pattern Analysis and Machine Intelligence 13, 583–598.

Xia, J., Miller, R.D., Park, C.B., 1999. Estimation of near-surface shear-wave velocity by inversion of Rayleigh waves. Geophysics 64 (3), 691–700.